Unveiling dislocation characteristics in Ni$_3$Al from stacking fault energy and ideal strength: A first-principles study via pure alias shear deformation

Shun-Li Shang [*], John Shimanek, Shipin Qin, Yi Wang, Allison M. Beese, and Zi-Kui Liu

Department of Materials Science and Engineering, The Pennsylvania State University, University Park, Pennsylvania 16802, USA

Nickel aluminide (Ni$_3$Al) is an important material for a number of applications, especially when used as a strengthening constituent in high-temperature Ni-based superalloys. Despite this, there is minimal information on its mechanical properties such as strength, plasticity, creep, fatigue, and fracture. In the present work, a first-principles based pure alias shear deformation has been applied to shed light on dislocation characteristics in Ni$_3$Al using the predicted stacking fault energy (i.e., the γ surface) and ideal shear strength (τ_{IS}). Results include direct evidence for the splitting of a $1/2[\bar{1}10]$ dislocation into two Shockley partials on the {111} plane, which is further supported by the equivalence of the complex stacking fault (CSF) energy γ_{CSF} and the antiphase boundary (APB) energy γ_{APB111}. Estimates of the Peierls stresses using τ_{IS} and elastic properties suggest the prevalence of edge dislocations in Ni and screw dislocations in Ni$_3$Al, agreeing with experimental observations regarding the dominance of edge dislocations in the first stage of crystal deformation in fcc metals and the yield-strength anomaly related to screw dislocations in Ni$_3$Al. The present calculations further point out that the CSF and APB111 are easily formed by shear due to the low-energy barriers, although the lowest planar energies are for the superlattice intrinsic stacking fault and the APB001. Through the case of Ni$_3$Al, the present work demonstrates that the pure alias shear methodology is not only computationally efficient but also provides valuable insight into the nature of shear-related properties.

I. INTRODUCTION

Shear deformation and associated properties such as stacking fault energy, γ, ideal (or theoretical) shear strength, τ_{IS}, and critical resolved shear stress (CRSS), τ_{CRSS}, are fundamental for understanding and modeling a vast number of materials properties and phenomena related to dislocations, plastic deformation, crystal growth, and phase transitions [1,2]. One example is the rise of yield strength with temperature, known as a yield-strength anomaly (YSA), that occurs in the presently studied Ni$_3$Al and other materials with the $L1_2$ structure [3,4]. It is generally agreed that the YSA occurs primarily due to thermally activated cross slip of screw dislocations from the {111} primary glide plane to the {001} cross-slip plane [5,6], where they remain locked in Kear-Wilsdorf (KW) configurations [7]. The occurrence of the YSA can be understood using energies in the γ surface of Ni$_3$Al—i.e., the energetic landscape of the generalized stacking fault energy [1]—including the antiphase boundary energy (γ_{APB111}), the complex stacking fault energy (γ_{CSF}), and the superlattice intrinsic stacking fault energy (γ_{SISF}) on the {111} slip plane, as well as the γ_{APB001} on the {001} cross-slip plane [3]. It is believed that the R value,

$$R = \gamma_{APB111}/\gamma_{APB001}, \qquad (1)$$

determines the driving force of cross slip to form KW locks [8], and the condition $R > \sqrt{3}$ indicates favorability of the

KW locks according to the Paidar-Pope-Vitek model [9]. In addition to the value of γ_{APB}, a low value of γ_{CSF} reduces thermal activation necessary for the formation of KW locks [3]. Besides providing an understanding for the YSA, energies in the γ surface can also be used to predict solid-solution strengthening and thermal cross-slip stress as shown for Mg alloys [10,11]; to explore twinnability as demonstrated for fcc and hcp metals [1,12]; and to study dislocation nucleation at a crack tip via the value of $\sqrt{\gamma_{US}}$ (where γ_{US} is the unstable stacking fault energy) according to the Rice criterion [13].

The ideal shear strength τ_{IS} is also fundamental to material behavior [1]. The value of τ_{IS} sets an upper bound on the attainable stress [14] related to such topics as (i) the minimum stress needed to plastically deform a perfect single crystal, (ii) the formation of a stacking fault, and (iii) materials strength and the extent of dislocation cores in a particular material [1,15]. Notably, τ_{IS} is a key parameter to estimate the Peierls stress—the force required to move an individual dislocation. The Peierls stress, τ_P, is approximately equal to τ_{CRSS} at 0 K [16]. For the case of a wide dislocation and according to Joós and Duesbery [17],

$$\tau_P = \frac{Kb}{a}\exp(-2\pi\zeta/a), \qquad (2)$$

where b is the Burgers vector, a the row spacing of atoms within the slip plane, K an elastic factor, and ζ the half-width of the dislocation with $\zeta = \frac{Kb}{4\pi\tau_{IS}}$. For an isotropic crystal, $K_{iso} = \mu\left(\frac{\sin^2\theta}{1-\nu} + \cos^2\theta\right)$ with μ being shear modulus, ν being Poisson's ratio, and θ the angle between the dislocation line

*Corresponding author: sus26@psu.edu

TABLE I. Calculated (Calc.) properties in Ni_3Al related to alias shear deformation in comparison with data in the literature (Expt., results at room temperature) including the stable and unstable stacking fault energies in mJ/m^2 (γ_S and γ_{US}, respectively), the ideal shear strength τ_{IS} in GPa, and the corresponding engineering strains ε [see its definition in Eq. (5)].

Shear	ε_S	γ_S	ε_{US}	γ_{US}	ε_{IS}	τ_{IS}	Notes and references
(111)[112]	0.20	203	0.13	229	0.12	3.7	Calc., this work, pure shear
CSF	0.20	212	0.14	254	0.10	5.1	Calc., this work, simple shear, relaxed
	0.20	252	0.14	284	0.07	2.2	Calc., this work, simple shear, unrelaxed
		205[a]		254			Calc., DFT, slab model [31]
		225					Calc., DFT [22]
		223					Calc., DFT+Peierls model [5]
		$120 \sim 218$					Calc., several EAM simulations [46]
		235 ± 40					Expt., weak-beam TEM images [3]
		206 ± 30					Expt., for alloy $Ni_{76}Al_{24}$ [3]
(111)[112]	0.47	72	0.23	1308	0.22	15.2	Calc., this work, pure shear
SISF	0.47	92	0.24	2273	0.14	9.4	Calc., this work, simple shear, unrelaxed
		75[a]		1368			Calc., DFT, slab model [31]
		80					Calc., DFT [22]
					0.32	13.7	Calc., DFT, not pure shear [32]
		79					Calc., DFT+Peierls model [5]
		$13 \sim 51$					Calc., several EAM simulations [46]
		6 ± 0.5					Expt., weak-beam TEM images [3]
		$10 \sim 276$					Expt., from several resources [43]
(111)[110]	0.16	205	0.119	230	0.12	4.2	Calc., this work, pure shear
APB111	0.41	215	0.272	582	0.12	7.6	Calc., this work, simple shear, relaxed
	0.41	314	0.214	1080	0.10	4.8	Calc., this work, simple shear, unrelaxed
		180[a]		778			Calc., DFT, slab model [31]
		178					Calc., DFT results at 100 K [33]
		210					Calc., DFT [22]
					0.18	5.8	Calc., DFT, not pure shear [32]
		172					Calc., DFT+Peierls model [5]
		$142 \sim 252$					Calc., several EAM simulations [46]
		175 ± 15					Expt., weak-beam TEM images [3]
		180 ± 20					Expt., for alloy $Ni_{76}Al_{24}$ [3]
		206 ± 22					Expt. [3]
						4.15	Expt. for dislocation-free Ni_3Al [49]
(001)[110]	0.37	64	0.17	1152	0.16	14.8	Calc., this work, pure shear
APB001	0.35	110	0.18	1200	0.15	14.8	Calc., this work, simple shear, relaxed
	0.35	119	0.19	2084	0.10	7.9	Calc., this work, simple shear, unrelaxed
		121					Calc., DFT+Peierls model [47]
		73					Calc., DFT results at 100 K [33]
		$74 \sim 102$					Calc., several EAM simulations [46]
		104 ± 15					Expt., weak-beam TEM images [3]
Unspecified						13.5	Expt., nanoindentation [44]
						~ 8	Expt., nanoindentation [28,45]
						18.8	Expt. plus Calc. (MD simulations) [46]

[a]Estimated values based on the published figures [31].

and its Burgers vector with $0°$ for screw dislocations and $90°$ for edge dislocations. The Peierls stress, τ_P, is hence essentially proportional to τ_{IS} based on Eq. (2). Furthermore, these stresses (τ_{IS}, τ_P, and/or τ_{CRSS}) are key inputs for continuum models such as finite-element and phase-field simulations to predict plastic deformation and recrystallization [18,19].

Determining stacking fault energy, γ, and ideal shear strength, τ_{IS}, from experiments is not a trivial task. Weak-beam transmission electron microscopy (TEM) images can be used to calculate γ values [3], and τ_{IS} values may be determined from well-controlled nanoindentation tests [20]. Relevant to the present Ni_3Al system, the measured γ values

using weak-beam TEM by Karnthaler *et al.* [3] are widely accepted (see the values in Table I). Karnthaler *et al.* [3] showed that the value of γ_{APB111} (175 ± 15 mJ/m^2) is in general lower than that of γ_{CSF} (235 ± 40 mJ/m^2). Based on the relationship between the γ values and the splitting of dislocations in fcc metals (e.g., Al, Cu, and Ni [15,21]), the inequivalent values of γ_{APB111} and γ_{CSF} by Karnthaler *et al.* [3] make it difficult to understand the splitting of $1/2[\bar{1}10]$ dislocation into two Shockley partials on the {111} plane [22],

$$\frac{1}{2}[\bar{1}10] \rightarrow \frac{1}{6}[\bar{2}11] + CSF + \frac{1}{6}[\bar{1}2\bar{1}]. \tag{3}$$

Note that direct observations of dislocation core splitting from first-principles based calculations can be made through the present pure alias shear deformation methodology as shown in Al and Cu [21], Ni [15], and Ni$_3$Al (this work). Additionally, core splitting can be observed using the lattice Green's function approach to explore equilibrium dislocation geometries and associated strength and ductility as demonstrated in Al [23,24], Fe [25], W [26], and Mg-Y alloy [27].

Regarding the ideal shear strength, τ_{IS}, it is generally believed that the τ_{IS} value of Ni$_3$Al (around 8 GPa) is roughly equal to that of Ni according to nanoindentation experiments [28]. This τ_{IS} value is in good agreement with the commonly accepted approximation that τ_{IS} is on the order of $\mu/10$ (shear modulus $\mu = 76$ GPa for Ni$_3$Al based on the measured elastic constants [29] and the Hill approach [30]). However, the predicted Peierls stress τ_P of Ni$_3$Al using $\tau_{IS} = 8$ GPa and Eq. (2) is at least one order of magnitude higher than experimental τ_{CRSS} values (see details in Sec. III B).

Unlike large uncertainties in estimating γ and τ_{IS} values from experiments, theoretical calculations are expected to simulate accurately shear deformation and associated properties. Existing calculations in Ni$_3$Al usually use the slab model (with vacuum) to estimate planar fault energies [31] and the non-pure shear deformation for stress [32]. The slab model results in smooth yet less insightful strain versus energy (or stress) curves [31,32] due to the deformation of atoms instead of lattice vectors during shear. This makes full relaxations (except for the one fixed angle required in pure shear deformation) difficult; see details about relaxations below. Predicted γ and τ_{IS} values from a slab model with insufficient relaxations (for example, $\gamma_{CSF} = 205$ mJ/m^2 and $\gamma_{APB111} = 180$ mJ/m^2 [33], and $\tau_{IS} = 5.8$ GPa for {111}⟨110⟩ shear [32]; see details in Table I) hence cannot provide more valuable insight into dislocation characteristics of Ni$_3$Al than the aforementioned experimental values.

It is worth mentioning that first-principles calculations based on density-functional theory (DFT) are usually performed at 0 K, but the predicted results are comparable to experimental data measured at room temperature (298 K) for many properties. For example, DFT calculations of enthalpy of formation (ΔH) for metal sulfides indicate that the difference of ΔH is negligible (<0.2 kJ/mol) between 0 K and room temperature [34]. Additionally, DFT calculations using the quasiharmonic approach show that the predicted bulk moduli of Ni and Ni$_3$Al decrease about 9 GPa (5%) from 0 K to room temperature [35], and the DFT-based quasistatic approach indicates that ideal shear strength of Ni decreases about 0.1 GPa (only 2%) [15]. Furthermore, Eq. (2) shows that Peierls stress, τ_P, increases with increasing ideal shear strength, τ_{IS}, but decreases with increasing elastic properties, implying the net change of τ_P value from 0 K to room temperature will be smaller than either individual effect. In the present work, all DFT calculations were performed at 0 K while all experimental data were gathered at room temperature.

Considering the significance of shear deformation and associated properties in Ni$_3$Al and the lack of detailed insights available in the literature, the present work aims to perform first-principles calculations of pure alias shear deformation, using the underlying science to unveil the relationship among stacking fault energy, ideal shear strength, and dislocation
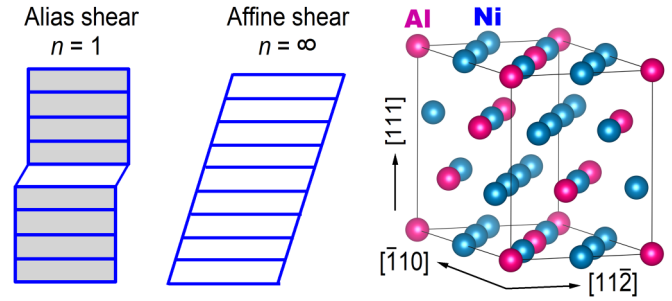

FIG. 1. Schematic diagrams of alias shear with atoms in one plane involved during the initial stage of shear (i.e., the number of involved atomic planes $n = 1$, shown as one unshaded area) and affine shear with atoms in all planes involved during the shear ($n = \infty$; all areas are unshaded), together with the 24-atom orthorhombic supercell of Ni$_3$Al with its lattice vectors parallel to the [11$\bar{2}$], [$\bar{1}$10], and [111] directions of the conventional $L1_2$ lattice.

characteristics in Ni$_3$Al. Unlike partial relaxations of the supercell used widely in the literature (such as in the slab model [31]), here, the pure shear deformation indicates that all relaxations, including cell shape, cell volume, and atomic positions, are allowed except for the fixed shear angle. Furthermore, in alias shear, only one atomic plane is involved in shear deformation while the other atoms initially remain in their original positions. The displacement then propagates through the supercell due to the interaction between the atoms during the shear processes [1,15,21]; see the schematic in Fig. 1 for the case of $n = 1$. In comparison to affine shear (where $n = \infty$ in Fig. 1), pure alias shear represents a deformation closer to actual shear processes [21], and generates both the γ surface and the ideal shear strength.

More insights can hence be gained, as shown in the present study of Ni$_3$Al where findings include (i) the direct observation of dislocation decomposition according to Eq. (3); (ii) the equivalent γ_{APB111} and γ_{CSF}; and (iii) the prevalence of screw dislocations in Ni$_3$Al based on the predicted τ_P using Eq. (2).

II. METHODOLOGY

A. Alias shear deformation of Ni$_3$Al

As schematically shown in Fig. 1, the alias shear with one sliding layer ($n = 1$), which is closer to the actual shear situations, was adopted in the present work to study Ni$_3$Al with $L1_2$ structure. By considering the dominant slip systems of {001}⟨110⟩ and {111}⟨110⟩ in Ni$_3$Al [36] as well as the splitting of 1/2[$\bar{1}$10] dislocation shown in Eq. (3), two supercells were built for the facility of first-principles calculations, namely, (i) a 16-atom tetragonal supercell with lattice vectors $\boldsymbol{a}_{tet}$, $\boldsymbol{b}_{tet}$, and $\boldsymbol{c}_{tet}$ of respective lengths $\sqrt{2}a_0$, $\sqrt{2}a_0$, and $2a_0$ (where a_0 is the lattice parameter of the $L1_2$ lattice) parallel to the [1$\bar{1}$0], [110], and [001] directions of the conventional $L1_2$ lattice; and (ii) a 24-atom orthorhombic supercell with lattice vectors $\boldsymbol{a}_{orth}$, $\boldsymbol{b}_{orth}$, and $\boldsymbol{c}_{orth}$ of respective lengths $\sqrt{6}a_0$, $\sqrt{2}a_0$, and $\sqrt{3}a_0$ parallel to the [11$\bar{2}$], [$\bar{1}$10], and [111] directions; see the orthorhombic supercell in Fig. 1. It is worth mentioning that the alias shear deformation of {001}⟨110⟩ generates the APB001 fault; the alias shear deformation of {111}⟨11$\bar{2}$⟩ along the easy and hard directions generates the

planar faults of CSF and SISF, respectively [14]; and the alias shear deformation of $\{111\}\langle\bar{1}10\rangle$ generates the APB111 fault.

After alias shear of the tetragonal or the orthorhombic supercell, the deformed lattice vector matrix $\bar{\mathbf{R}}$ can be expressed by [1,15]

$$\bar{\mathbf{R}} = \mathbf{RD}, \tag{4}$$

where $\mathbf{R}$ is the undeformed lattice vector matrix, and $\mathbf{D}$ the deformation matrix. For example, the $\mathbf{D}$ matrices for the $\{111\}\langle11\bar{2}\rangle$ and $\{111\}\langle\bar{1}10\rangle$ shears of the aforementioned orthorhombic supercell are as follows:

$$\mathbf{D}_{\langle11\bar{2}\rangle} = \begin{bmatrix} 1 & 0 & 0 \\ 0 & 1 & 0 \\ \varepsilon & 0 & 1 \end{bmatrix} \quad \text{and} \quad \mathbf{D}_{\langle\bar{1}10\rangle} = \begin{bmatrix} 1 & 0 & 0 \\ 0 & 1 & 0 \\ 0 & \varepsilon & 1 \end{bmatrix}, \tag{5}$$

where ε is the shear magnitude corresponding to the engineering shear strain, i.e., the ratio of shear displacement with respect to the height of the supercell [1,15]. In the present practice of first-principles calculations, Cartesian coordinates for the initial atomic positions were employed for the facility of alias shear deformation [1,15,21]. Pure shear deformations, including relaxations of atomic positions, cell shape, and cell volume except for the fixed shear angle, were performed by an external PYTHON optimizer GADGET developed by Bučko *et al.* [37] to control first-principles calculations of both stresses and forces acting on each atom. Note that the alias shear deformation employs only half atoms (and no vacuum layers) in the supercell in contrast to the slab model, making alias shear more computationally efficient to study shear-related properties.

B. First-principles calculations

All first-principles calculations in the present work were performed by the Vienna *Ab initio* Simulation Package (VASP) [38] together with the ion-electron interaction described by the projector augmented wave method [39]. The exchange-correlation functional was depicted by the generalized gradient approximation [40], the same potential as our previous first-principles calculations for Ni-based alloys [2,15,41]. The core configurations recommended by VASP were adopted in the present work, i.e., [Ne] for Al and [Ar] for Ni. During VASP calculations, the k-point meshes of $4\times7\times6$ were used for the 24-atom orthorhombic supercell (or $8\times8\times6$ for the 16-atom tetragonal supercell) and a cutoff energy of 270 eV was employed for the plane-wave basis set according to our trial calculations. The energy convergence criterion of electronic self-consistency was selected as 10^{-5} eV per supercell for all calculations. The reciprocal-space energy integration was performed by the Methfessel-Paxton [42] technique with a 0.2 eV smearing width, which results in accurate total energies as well as stresses. Concerning pure shear deformation, all relaxed stress components except for the one corresponding to the fixed shear angle were less than 0.15 GPa, and the forces acting on atoms were less than 0.03 eV/Å. Besides the present focus of pure alias shear, two more ancillary shear deformations were also employed for comparison: the simple alias shear without relaxations of the supercell (represented by "simple" for short) and the simple alias shear with relaxations of atomic positions only (represented by "simple+RX" for

short). In addition, spin polarization was considered in all DFT calculations due to the magnetic nature of Ni.

III. RESULTS AND DISCUSSION

A. Shear-related properties in Ni$_3$Al

Figures 2 and 3 illustrate the variations of planar fault energy γ, shear stress τ, and spin magnetic moment of Ni$_3$Al during the alias shear deformations of $\{111\}\langle11\bar{2}\rangle$, $\{111\}\langle\bar{1}10\rangle$, and $\{001\}\langle110\rangle$. These two figures show that only the simple shear gives smooth energy and stress curves while the relaxations (pure shear or simple+RX) lead to sudden changes of energy around the unstable shear positions, corresponding to the zero stress and the unstable stacking fault energy (γ_{US}). Furthermore, the maximum stress gives the ideal shear strength τ_{IS} and the local minimum in energy curve gives the stable stacking fault energy (γ_S). The present γ_S, γ_{US}, and τ_{IS} values as well as the corresponding engineering strains shown in Figs. 2 and 3 are also listed in Table I. In general, the present predictions are in good agreement with experimental estimations [3,28,43–46] and other DFT and embedded-atom method (EAM) calculations [5,22,31–33,46,47]; see details in Table I. For example, the present γ_{CSF} values (203 mJ/m^2 from pure shear and even 212 and 252 mJ/m^2 from simple shears) agree well with the previous calculations (120 ~ 225 mJ/m^2) [5,22,31,46] and experiments (206 ~ 235 mJ/m^2) [3] with large uncertainties. Among the γ_S and γ_{US} values related to CSF, SISF, APB111, and APB001 (cf. Table I), it is found that the lower γ_S values relate to the formation of SISF (72 mJ/m^2 from pure shear) and APB001 (64 mJ/m^2 from pure shear), matching reasonably well the previous simulations ($\gamma_{SISF} = 13 \sim 80$ mJ/m^2 and $\gamma_{APB001} = 73 \sim 121$ mJ/m^2) and experiments ($\gamma_{SISF} = 6 \sim 276$ mJ/m^2 and $\gamma_{APB001} = 104$ mJ/m^2). Despite the lower γ_{SISF} and γ_{APB001} values, shear deformations to form SISF and APB001 are difficult due to the large energy barriers, e.g., $\gamma_{US} > 1000$ mJ/m^2 based on pure shear deformation.

It is interesting to find that the stable (as well as the unstable) stacking fault energies related to the formation of CSF and APB111 from pure alias shear are almost identical, which is contrary to the experimental results by Karnthaler *et al.* [3], *viz.*, $\gamma_{CSF} \approx \gamma_{APB111}$ (203 ~ 205 mJ/m^2) and the γ_{US} values ~230 mJ/m^2 for both faults (cf. Table I), providing indirect evidence about the splitting of $1/2[\bar{1}10]$ dislocation in terms of Eq. (3) (see more discussion in Sec. III B). The lower γ_{US} value (~230 mJ/m^2 to form CSF and APB111 compared to $\gamma_{US} > 1000$ mJ/m^2 to form SISF and APB001) indicates that both CSF and APB111 are easy to be formed by shear.

The ideal shear strength τ_{IS} is in general proportional to the unstable stacking fault energy γ_{US} (see Table I, Figs. 2, and 3), indicating the degree of difficulty to form a planar fault by shear in the present work. It should be mentioned that the τ_{IS} value is inversely proportional to the number of layers in the supercell [48]. Considering the limited layers (such as one layer) involved in actual shear deformation, the minimum of three {111} layers is employed for both the tetragonal and orthorhombic supercells of the $L1_2$ lattice in the present work, corresponding to the highest τ_{IS} value to be obtained for a given shear deformation [48]. It is seen that the lowest τ_{IS} value in Ni$_3$Al (3.7 GPa by pure shear) is related
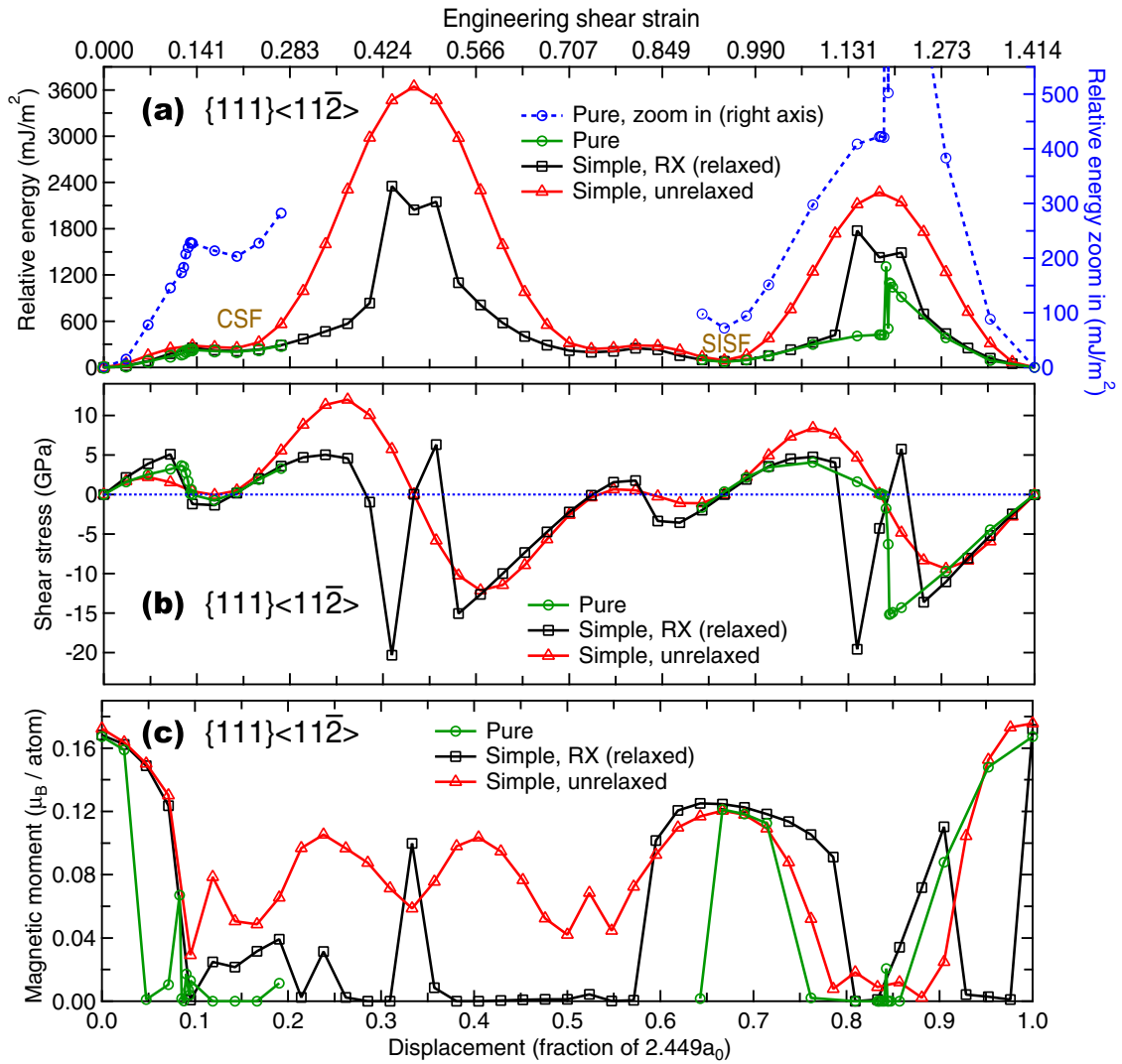
FIG. 2. Variations of (a) relative energy, i.e., the γ surface, (b) shear stress, τ, and (c) magnetic moment of Ni$_3$Al in terms of $\{111\}\langle11\bar{2}\rangle$ alias shear using different shear schemes, including pure shear and simple shears with and without relaxations, where a_0 is the lattice parameter of the $L1_2$ lattice.

to the formation of CSF, followed by $\tau_{IS} = 4.2$ GPa to form APB111. However, the τ_{IS} values are quite high ($\sim$15 GPa) to form SISF and APB001, agreeing with the higher γ_{US} values to form these faults. The present τ_{IS} values (3.7, 4.2, 14.8, and 15.2 GPa from different pure shear deformations) are in good agreement with the estimates from compressive strength of dislocation-free nanocube (4.15 GPa) [49], nanoin-dentation experiments ($\sim$8 and 13.5 GPa) [28,44,45], and molecular-dynamic simulations (16.5 $\sim$ 18.8 GPa) [46]; see details in Table I. Especially the present τ_{IS} value (4.2 GPa from $\{111\}\langle\bar{1}10\rangle$ pure shear) agrees well with the estimated resolved shear stress of 4.15 GPa according to the measured compressive strength by assuming a $\{111\}\langle110\rangle$ slip [49]. It is worth mentioning that the lowest τ_{IS} value of Ni$_3$Al (3.7 GPa in the present work) is lower than that of pure Ni (5.1 GPa based on pure shear deformation [15]) due to the soft nature of Al compared to Ni (e.g., bulk moduli 74 vs 196 GPa based on DFT calculations [50]).

The degree of difficulty regarding shear deformation can be qualitatively understood via the distribution of differential

charge density, $\Delta\rho$ [1,2,41,51,52]. The $\Delta\rho$ is defined as the charge-density difference with respect to the reference (or noninteracting) charge density, which is determined by DFT calculations of one electronic step in the present work [1]. Based on density-functional theory, the denser the $\Delta\rho$ values, the stronger the bonding between atoms. Therefore, the anisotropic $\Delta\rho$ corresponds to anisotropic properties such as elasticity in fcc Al [52], and the nonspherical distribution of $\Delta\rho$ hinders shear deformation due to the difficulty of charge redistribution, resulting in higher stacking fault energies and ideal shear strengths. As an example, Fig. 4 shows the $\Delta\rho$ contour maps of Ni$_3$Al during the simple alias shear along $\{111\}\langle11\bar{2}\rangle$. The $\Delta\rho$ around each Ni displays a cube-shaped distribution, implying the difficulty of shear deformation. During shear deformation from Figs. 4(a) to 4(d), the Ni-3 atom, for instance, approaches Ni-4, resulting in the re-distribution of $\Delta\rho$ and an increasing stacking fault energy and shear stress. The shear position in Fig. 4(d) roughly corresponds to the maximum (unstable) stacking fault energy γ_{US}.
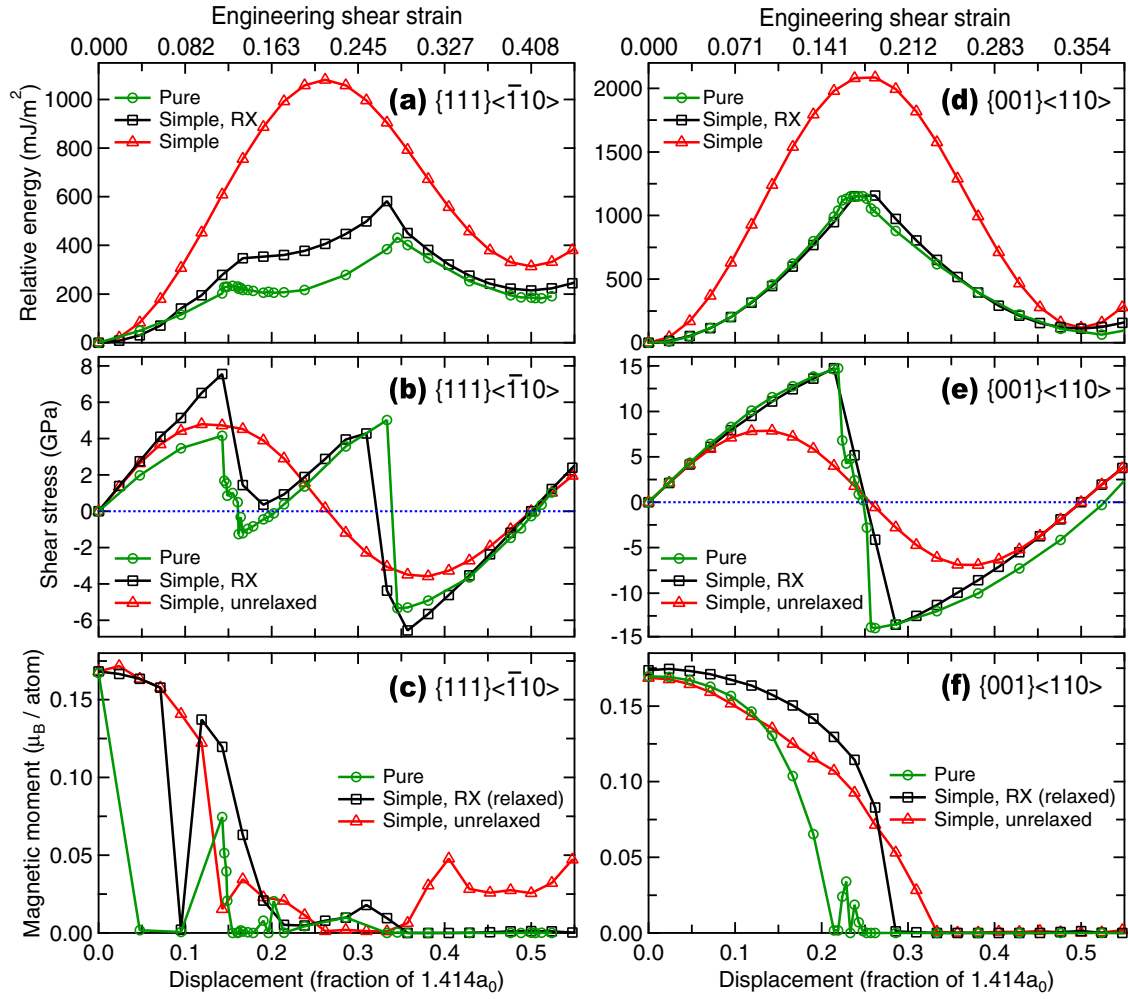
FIG. 3. Variations of (a), (d) relative energy, i.e., the γ surface, (b), (e) shear stress, τ, and (c), (f) magnetic moment of Ni_3Al based on the alias shear deformations of $\{111\}\langle\bar{1}10\rangle$ and $\{001\}\langle110\rangle$ using different shear schemes, including pure shear and simple shears with and without relaxations, where a_0 is the lattice parameter of the $L1_2$ lattice.

Furthermore, the magnetic moment of Ni_3Al is relatively small ($<0.17\,\mu_B$/atom); see Figs. 2(c) and 3(c). In general, the magnetic moment of Ni_3Al decreases with increasing shear displacement and appears scattered as a function of applied strain due mainly to the sudden change of stress and energy (as well as volume, not shown here) near the regions of ideal shear strength and unstable stacking fault energy. Figures 2(c) and 3(c) show that the magnetic moments
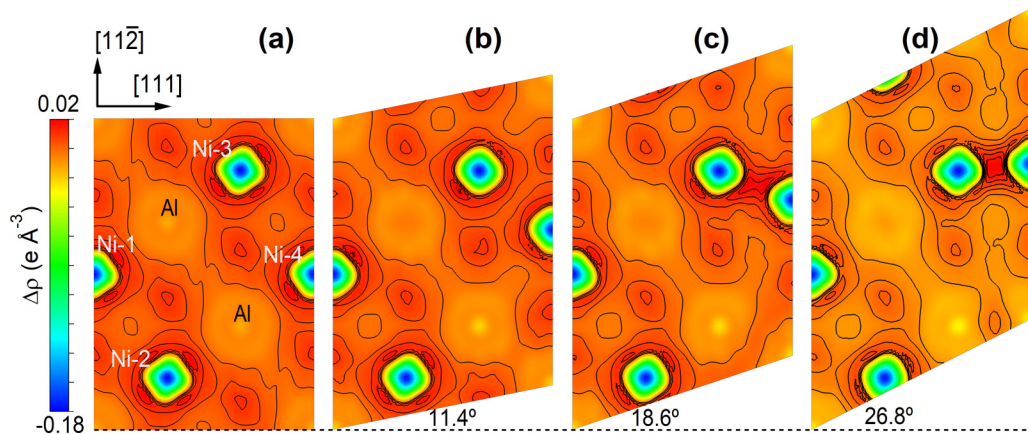

FIG. 4. Contour maps of differential charge density ($\Delta\rho$, in unit of e/Å^3) during the $\{111\}\langle11\bar{2}\rangle$ simple alias shear of Ni_3Al from the initial configuration (a) to the configuration (d) with the highest shear stress.
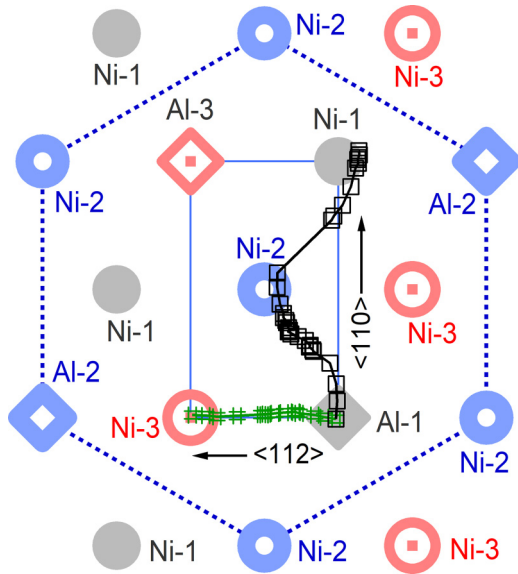
FIG. 5. Movement of an Al atom located at the Al-1 position of the {111} plane (layer-1) adjacent to the stacking fault plane during the pure alias shear deformations of {111}⟨$\bar{1}$10⟩ (from the Al-1 to Ni-1 position) and {111}⟨11$\bar{2}$⟩ (from the Al-1 to Ni-3 position). The numbers 1, 2, and 3 indicate three {111} layers of Ni$_3$Al.

of Ni$_3$Al are close to zero ($<0.04 \, \mu_\text{B}$/atom) in most shear positions, especially for the cases with relaxations (pure shear and simple+RX). Note that the near-zero magnetic moment has negligible influence on the resulting total energy and stress, and hence the scattered magnetic moments are not further examined with respect to such potential factors as k-point mesh density, which was found to be significant in the cases of LaNi$_5$ and LaNi$_5$H$_7$ [53].

B. Applications of shear-related properties and dislocation characteristics in Ni$_3$Al

As an example, Fig. 5 shows the movement of one Al atom (see Al in the original Al-1 position) on the stacking fault plane (here the number 1 after Al or Ni indicates the stacking fault plane, 2 and 3 indicate the other planes) during (a) the pure alias shear of {111}⟨11$\bar{2}$⟩ to generate the CSF (see the black □ symbols to the Ni-1 position) and (b) the pure alias shear along {111}⟨$\bar{1}$10⟩ to generate the APB111 (see the green # symbols to the Ni-3 position). It can be seen that the movement of Al during the pure alias shear of {111}⟨11$\bar{2}$⟩ is almost along the straight line from Al-1 to Ni-3. However, the movement of Al during the pure alias shear of {111}⟨$\bar{1}$10⟩ is along two {111}⟨11$\bar{2}$⟩ directions from Al-1 to Ni-2 and then to Ni-1, i.e., the movement of Al shows directly the splitting of a 1/2[$\bar{1}$10] dislocation into two Shockley partials on the {111} plane as indicated by Eq. (3). Note that the other atoms in the stacking fault plane show almost the same behaviors as that of Al in the Al-1 position.

To further examine the splitting of the 1/2[$\bar{1}$10] dislocation, Fig. 6 shows the variations of lattice parameters and angles between them during the pure alias shear of {111}⟨$\bar{1}$10⟩ in the orthorhombic supercell (see Fig. 1). In the initial stage of shear up to the engineering shear strain of 0.11, the

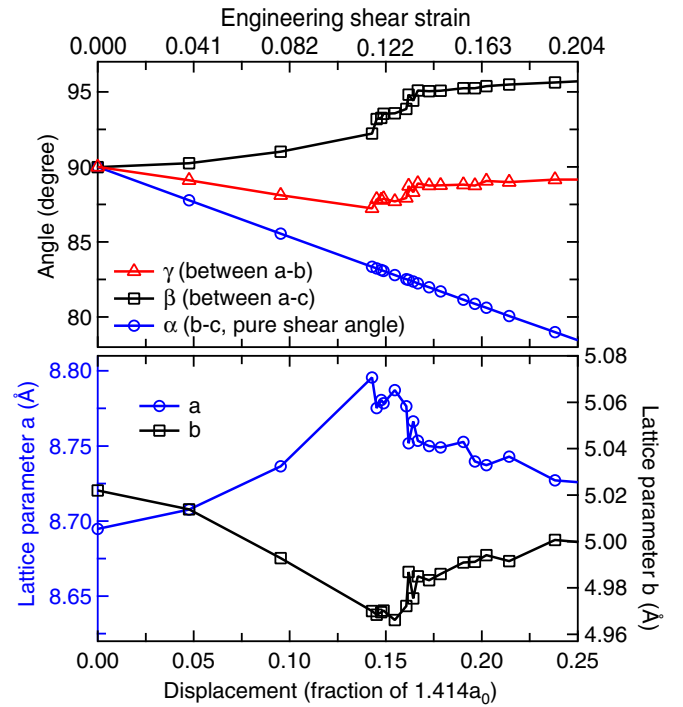FIG. 6. Variations of lattice parameters (a), (b), and (c) and their angles (α, β, and γ) during the pure alias shear deformation of {111}⟨$\bar{1}$10⟩ for the orthorhombic supercell of Ni$_3$Al; see Fig. 1.

lattice parameters and angles change smoothly (see Fig. 3). Around an engineering shear strain of 0.11, sudden changes in the lattice parameters occur due to reaching the ideal shear strength and unstable stacking fault energy (see Fig. 3) which also coincides with a direction change in atomic movements (see Fig. 5). The sudden fluctuations of lattice parameters and angles signal dislocation splitting and the appearances of γ_US and τ_IS during pure alias shear deformation.

The predicted τ_IS value can be used to estimate Peierls stress τ_P according to Eq. (2). In contrast to the elastic factor K_iso for an isotropic crystal as in Eq. (2), the elastic factor K of an anisotropic crystal is direction dependent. For an edge dislocation aligned with the z direction with a Burgers vector $\mathbf{b} = (b_x, b_y, 0)$, the K_{e_x} along the x direction is given by [54]

$$K_{e_x} = (\bar{c}'_{11} + c'_{12}) \left[\frac{c'_{66}(\bar{c}'_{11} - c'_{12})}{(\bar{c}'_{11} + c'_{12} + 2c'_{66})c'_{22}} \right]^{1/2}, \quad (6)$$

where $\bar{c}'_{11} = (c'_{11}c'_{22})^{1/2}$, and the c'_{ij} represents the transformed elastic constants onto the slip system of interest. In the present orthorhombic supercell shown in Fig. 1, for example, the transformed lattice vectors are parallel to the [11$\bar{2}$], [$\bar{1}$10], and [111] directions. Note that for the present Ni$_3$Al cell shown in Fig. 1, $K_{e_x} = K_{e_y} (= K_e)$ for edge dislocations along both the x- and y directions. In addition, the elastic factor K_s for screw dislocations of an anisotropic crystal can be expressed as [54]

$$K_s = \left(c'_{44} c'_{55} - c'^2_{45} \right)^{1/2}. \quad (7)$$

By means of Eq. (2) [as well as Eqs. (6) and (7)] with input of the minimum $\tau_\text{IS} = 3.7$ GPa for Ni$_3$Al (cf. Table I) and the

TABLE II. Calculated Peierls stresses (τ_P, MPa) at 0 K for four cases of edge (e) and screw (s) dislocations using elastic factors for isotropic (iso) and anisotropic (aniso) crystals in comparison with experimental CRSS values (τ_{CRSS}, MPa) at room temperature for both Ni$_3$Al and Ni.

Material	τ_P (iso-e)	τ_P (iso-s)	τ_P (aniso-e)	τ_P (aniso-s)	Experimental τ_{CRSS}
Ni$_3$Al[a]	0.7[b]	14.2[b]	0.4[b]	75.0[b]	27 ± 5,[e] 75 ± 20,[f] 40–90[g]
	3.0[c]	38.6[c]	1.8[c]	161.8[c]	
	1088[d]	0.4[d]			
Ni[a]	19.2[b]	168.7[b]	14.4[b]	374.5[b]	5.7,[h] 5.9 ∼ 8.3,[i] 9.9,[j] 10.2,[k] 17.5[l]
	49.7[c]	327.5[c]	38.5[c]	651.0[c]	

[a]Elastic constants (c_{ij}) and lattice parameters a_0 to predict τ_P by Eq. (2) were taken from our previous DFT calculations, i.e., $c_{11} = 242$ GPa, $c_{12} = 152$ GPa, $c_{44} = 125$ GPa, and $a_0 = 3.57$ Å for Ni$_3$Al [55]; and $c_{11} = 273$ GPa, $c_{12} = 160$ GPa, $c_{44} = 114$ GPa, and $a_0 = 3.52$ for Ni [48].

[b]The lowest τ_{IS} values of $\{111\}\langle11\bar{2}\rangle$ slip were used to predict τ_P, i.e., $\tau_{IS} = 3.7$ GPa for Ni$_3$Al (see Table I) and $\tau_{IS} = 5.1$ GPa for Ni [15].

[c]The second lowest τ_{IS} values of $\{111\}\langle\bar{1}10\rangle$ slips were used to predict τ_P, i.e., 4.2 GPa for Ni$_3$Al (see Table I) and 5.8 GPa for Ni [15].

[d]For reference only using the Poisson's ratio (estimated by c_{ij} values and the Voigt approach) to predict the half-width of dislocation and then τ_P.

[e]CRSS value for Ni$_3$Al sample with 78 at. % Ni and 22 at. % Al as well as 0.2% plastic strain [3].

[f]CRSS value of tensile tests for Ni$_3$Al samples with 77 at. % Ni and 23 at. % Al for (111)[110] slip [60].

[g]Orientation-dependent CRSS values of Ni$_3$Al alloys [61].

[h]CRSS value of Ni measured in 1933 [56].

[i]CRSS value of Ni measured in 1958 [57].

[j]CRSS value of Ni measured in 2016 [69].

[k]CRSS value of Ni measured in 1951 [58].

[l]CRSS value of Ni measured in 2005 [59].

DFT-predicted elastic constants of Ni$_3$Al [55], the predicted τ_P values for both the edge (e) and screw (s) dislocation cases of Ni$_3$Al using both the isotropic (iso) and anisotropic (aniso) elastic factors are given in Table II (i.e., predictions of four cases: iso-e, iso-s, aniso-e, and aniso-s). For the sake of comparison, the predicted τ_P values of fcc Ni and the measured CRSS values at room temperatures for both Ni [56–59] and Ni$_3$Al [3,60,61] are also listed in Table II and plotted in Fig. 7. All the required data to predict τ_P values of
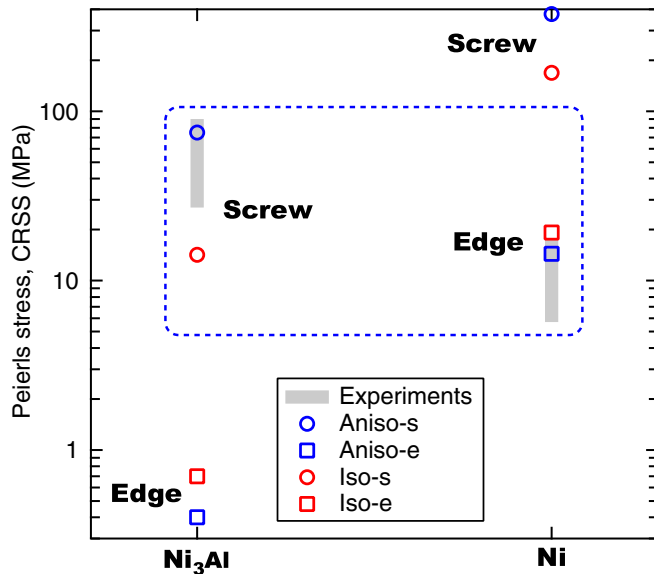

FIG. 7. Calculated Peierls stresses at 0 K for four cases of edge (e) and screw (s) dislocations using elastic factors for isotropic (iso) and anisotropic (aniso) crystals in comparison with experimental CRSS values at room temperature for Ni$_3$Al and Ni; see the detailed values in Table II.

Ni$_3$Al and Ni are detailed as footnotes of Table II, including τ_{IS}, c_{ij}, and lattice parameters [15,55]. Table II and Fig. 7 show that the range of the predicted τ_P values for anisotropic crystal from edge to screw dislocations (blue symbols) is larger than that of the isotropic crystal from edge to screw dislocations (red symbols) for both Ni$_3$Al and Ni. It is seen that the predicted τ_P values of Ni$_3$Al are smaller than those of Ni due mainly to the smaller τ_{IS} used for Ni$_3$Al (3.7 GPa vs. 5.1 GPa for Ni$_3$Al and Ni, respectively; see Table II). It can be seen that the τ_P values of Ni$_3$Al for screw dislocations (circular symbols) and the τ_P values of Ni for edge dislocations (square symbols), especially the values for anisotropic cases (the blue symbols), agree reasonably well with experimental CRSS values (which are scattered; see the filled gray bars as well as the values in Table II). This comparison of calculated τ_P values and experimental CRSS values indicates the predominance of screw dislocations in Ni$_3$Al and edge dislocations in Ni. In terms of experimental observations, the edge dislocation dipoles that are prevalent in stage I of fcc single-crystal deformation can be explained by mutual annihilation of screw segments through cross slip [3,62]. It was observed that Ni$_3$Al exhibits long and straight screw dislocations, adopting either incomplete or complete KW locking configurations, while the edge dislocations mainly act as links between the long screw dislocations and their cross-slipped parts [6,36]. It was further observed that deformation of Ni$_3$Al-based superalloy is dominated by screw dislocations in the early stage of tensile tests using different strain levels (from 0.8 to 8.2%) [63]. Similarly to Ni, the τ_P values of Ni$_3$Al from edge dislocations are lower than those from screw dislocations (see Fig. 7), indicating plastic deformation should start from the easy deformed edge dislocations for both Ni and Ni$_3$Al. Experimentally it was observed that the mobile edge dislocations (instead of the sessile screw dislocations) contribute most to the primary creep strain in Ni$_3$Al [64,65]. Here, the commonly observed

screw dislocations in Ni_3Al [6,36,63] may be due to (i) the not enough active edge dislocations to initiate plastic deformation, (ii) the easy trigger of screw dislocations during plastic deformation, and/or (iii) the less accurate Peierls stresses predicted in the present work. Detailed dislocation mechanism in Ni_3Al can be explored using such as the crystal plasticity finite-element simulations [48,63,66], but this study is beyond the scope of the present work.

The agreement between the present predictions and experimental observations on dislocation types (Table II and Fig. 7) indicates that it is reasonable to select the minimum τ_{IS} value in Ni_3Al to predict τ_P. It is worth mentioning that the lower τ_P values in Ni_3Al can be increased by using higher τ_{IS} values. For example, from $\tau_{IS} = 3.7\,\text{GPa}$ (to generate the CSF) to $4.2\,\text{GPa}$ (to generate the APB111) by considering the dominant slip system of $\{111\}\langle110\rangle$ in Ni_3Al [36], the predicted τ_P values increase about 2.2 to 4.5 times, and the predicted τ_P values of screw dislocations ($38.6 \sim 161.8\,\text{MPa}$) are still in a good agreement with experimental τ_{CRSS} values ($27 \sim 90\,\text{MPa}$); see detailed values in Table II.

It is found that τ_{IS} is a key value to predict the half-width of dislocation ζ and hence the Peierls stress, τ_P, by using Eq. (2). As an example of the use of inaccurate values, the predicted τ_P is 372 MPa for an isotropic edge dislocation using $\tau_{IS} = 8\,\text{GPa}$ estimated from nanoindentation [28], and the predicted τ_P is 1088 MPa for an isotropic edge dislocation using the ζ value from Poisson's ratio ν via $\zeta = \frac{d}{2(1-\nu)}$ (where d is the distance between slip planes). These τ_P values (372 and 1088 MPa) are at least one and even two orders of magnitude higher than experimental τ_{CRSS} values at room temperature ($27 \sim 90\,\text{MPa}$; see Table II), supporting the observations that the predicted Peierls stress is less accurate by using less accurate τ_{IS} such as the one estimated from the γ surface [67]. It was further observed that the calculated Peierls stress can be improved by allowing strain-field relaxation in the process of overcoming the Peierls potential [68].

In addition to predicting Peierls stress from τ_{IS}, the γ surface is also fundamental to understand and model numerous material properties and phenomena as mentioned in Sec. I. For example, the presently predicted R value [see Eq. (1)] is 3.2 based on the pure alias shear deformation. As this R value is greater than $\sqrt{3}$, this indicates the possibility of forming KW locks in Ni_3Al [9]. Additionally, the D value, defined as the ratio of surface energy to unstable stacking fault energy as $D = \gamma_{surface}/\gamma_{US}$, can be used to determine the ductility by using the Rice criterion [13]. The presently predicted value of D is 16.2 using the values of $\gamma_{US} = 229\,\text{mJ/m}^2$ to generate the CSF (see Table I) and $\gamma_{surface} = 3705\,\text{mJ/m}^2$ [31]; in contrast, $D = 2.8$ using the values of $\gamma_{US} = 1308\,\text{mJ/m}^2$ to generate the SISF (see Table I). It is therefore meaningful to predict the influence of alloying elements on the R, D, and τ_P values of Ni_3Al or other $L1_2$ alloys to understand trends and design alloys. In addition, the presently employed methodology of pure alias shear provides not only a simple and accurate way to calculate shear-related properties but also gives valuable insight into dislocation characteristics.

IV. SUMMARY

The present work investigates shear-related properties with a focus on dislocation characteristics in Ni_3Al by means of a computationally efficient methodology of pure alias shear. The present first-principles results provide direct evidence concerning the splitting of the $1/2[\bar{1}10]$ dislocation into two Shockley partials on the $\{111\}$ plane [cf. Eq. (3)], and this splitting is further supported by the equivalent planar fault energies of γ_{CSF} and γ_{APB111} predicted by the pure alias shears on the $\{111\}$ plane. Comparing the predicted Peierls stresses τ_P with experimental τ_{CRSS}, the present work suggests the prevalence of screw dislocations in Ni_3Al as well as edge dislocations in Ni due to the fact that the minimum ideal shear strength of Ni_3Al is about 30% lower than that of Ni (3.7 vs 5.1 GPa).

In addition, the present dislocation characteristics agree well with experimental observations regarding (a) the dominant edge dislocations in stage I of fcc single-crystal deformation; and (b) the yield-strength anomaly (YSA) in Ni_3Al related to screw dislocations adopting the Kear-Wilsdorf configurations [7]. Note that the YSA also can be understood by means of empirical relationships in the literature (see the Introduction) and the presently predicted planar fault energies, ideal shear strengths, and Peierls stresses (i.e., the CRSS values at low temperatures). It is further observed that the planar faults of CSF and APB111 are easily formed by shear due to the lower energy barriers (both the lower ideal shear strength and the lower unstable stacking fault energy as shown in Table I), although even lower planar fault energies are found for SISF and APB001. The present predictions of ideal shear strength and stacking fault energy are in favorable accord with the scattered results from experiments and other calculations. However, only the present predictions—from the pure alias shear deformation—provide more insights into the underlying science of Ni_3Al dislocation splitting and dislocation character than, for example, the commonly employed slab model. Beyond the present work, we also can explore more properties of Ni_3Al such as (i) temperature-dependent Peierls stress in Ni_3Al by means of the quasistatic approach [15]; (ii) solute strengthening in Ni_3Al by predicting the effect of alloying elements on Peierls stress (i.e., the CRSS value) using Eq. (2); and (iii) stress versus strain curve through the combination of Peierls stress and finite-element simulations [48].

[1] S. L. Shang, W. Y. Wang, B. C. Zhou, Y. Wang, K. A. Darling, L. J. Kecskes, S. N. Mathaudhu, and Z. K. Liu, Acta Mater. **67**, 168 (2014).

[2] S. L. Shang, C. L. Zacherl, H. Z. Fang, Y. Wang, Y. Du, and Z. K. Liu, J. Phys.: Condens. Matter **24**, 505403 (2012).

[3] H. P. Karnthaler, E. T. Mühlbacher, and C. Rentenberger, Acta Mater. **44**, 547 (1996).

[4] Y. Umakoshi, D. P. Pope, and V. Vitek, Acta Metall. **32**, 449 (1984).

[5] G. Schoeck, S. Kohlhammer, and M. Fahnle, Philos. Mag. Lett. **79**, 849 (1999).

[6] Y. M. Wang-Koh, Mater. Sci. Technol. **33**, 934 (2017).

[7] B. H. Kear and H. G. F. Wilsdorf, Trans. Metall. Soc. AIME **224**, 382 (1962).

[8] Y. Abate, S. Gamage, Z. Li, V. Babicheva, M. H. Javani, H. Wang, S. B. Cronin, and M. I. Stockman, Light Sci. Appl. **5**, e16162 (2016).

[9] V. Paidar, D. Pope, and V. Vitek, Acta Metall. **32**, 435 (1984).

[10] J. A. Yasi, L. G. Hector, and D. R. Trinkle, Acta Mater. **59**, 5652 (2011).

[11] J. A. Yasi, L. G. Hector, and D. R. Trinkle, Acta Mater. **60**, 2350 (2012).

[12] N. Bernstein and E. B. Tadmor, Phys. Rev. B **69**, 094116 (2004).

[13] J. R. Rice, J. Mech. Phys. Solids **40**, 239 (1992).

[14] Y.-L. Liu, Y. Zhang, H.-B. Zhou, G.-H. Lu, and M. Kohyama, J. Phys.: Condens. Matter **20**, 335216 (2008).

[15] S. L. Shang, W. Y. Wang, Y. Wang, Y. Du, J. X. Zhang, A. D. Patel, and Z. K. Liu, J. Phys.: Condens. Matter **24**, 155402 (2012).

[16] P. Cordier, J. Amodeo, and P. Carrez, Nature (London) **481**, 177 (2012).

[17] B. Joós and M. S. Duesbery, Phys. Rev. Lett. **78**, 266 (1997).

[18] A. Gaubert, Y. Le Bouar, and A. Finel, Philos. Mag. **90**, 375 (2010).

[19] C. Zambaldi, F. Roters, D. Raabe, and U. Glatzel, Mater. Sci. Eng.: A **454–455**, 433 (2007).

[20] J. Li, MRS Bull. **32**, 151 (2007).

[21] M. Jahnátek, J. Hafner, and M. Krajčí, Phys. Rev. B **79**, 224103 (2009).

[22] O. N. Mryasov, Y. N. Gornostyrev, M. van Schilfgaarde, and A. J. Freeman, Acta Mater. **50**, 4545 (2002).

[23] C. Woodward, D. R. Trinkle, L. G. Hector, and D. L. Olmsted, Phys. Rev. Lett. **100**, 045507 (2008).

[24] G. P. M. Leyson, W. A. Curtin, L. G. Hector, and C. F. Woodward, Nat. Mater. **9**, 750 (2010).

[25] M. R. Fellinger, A. M. Z. Tan, L. G. Hector, Jr., and D. R. Trinkle, Phys. Rev. Mater. **2**, 113605 (2018).

[26] Y.-J. Hu, M. R. Fellinger, B. G. Bulter, Y. Wang, K. A. Darling, L. J. Kecskes, D. R. Trinkle, and Z.-K. Liu, Acta Mater. **141**, 304 (2017).

[27] D. Buey, L. G. Hector, and M. Ghazisaeidi, Acta Mater. **147**, 1 (2018).

[28] J. Pokluda, M. Černý, M. Šob, and Y. Umeno, Prog. Mater. Sci. **73**, 127 (2015).

[29] J. Frankel, J. Vassiliou, J. C. Jamieson, D. P. Dandekar, and W. Scholz, Phys. B+C **139–140**, 198 (1986).

[30] R. Hill, Proc. Phys. Soc. Sect. A **65**, 349 (1952).

[31] X.-X. Yu and C.-Y. Wang, Mater. Sci. Eng. A **539**, 38 (2012).

[32] Y.-J. Wang and C.-Y. Wang, Scr. Mater. **61**, 197 (2009).

[33] V. R. Manga, S.-L. Shang, W. Y. Wang, Y. Wang, J. Liang, V. H. Crespi, and Z.-K. Liu, Acta Mater. **82**, 287 (2015).

[34] S.-L. Shang, Y. Wang, T. J. Anderson, and Z.-K. Liu, Phys. Rev. Mater. **3**, 015401 (2019).

[35] S.-L. Shang, Y. Wang, D. Kim, and Z.-K. Liu, Comput. Mater. Sci. **47**, 1040 (2010).

[36] P. R. Bhowal and M. Metzger, Metall. Trans. A **9**, 1027 (1978).

[37] T. Bučko, J. Hafner, and J. G. Ángyán, J. Chem. Phys. **122**, 124508 (2005).

[38] G. Kresse and J. Furthmüller, Phys. Rev. B **54**, 11169 (1996).

[39] G. Kresse and D. Joubert, Phys. Rev. B **59**, 1758 (1999).

[40] J. P. Perdew, J. A. Chevary, S. H. Vosko, K. A. Jackson, M. R. Pederson, D. J. Singh, and C. Fiolhais, Phys. Rev. B **46**, 6671 (1992).

[41] S. L. Shang, D. E. Kim, C. L. Zacherl, Y. Wang, Y. Du, and Z. K. Liu, J. Appl. Phys. **112**, 053515 (2012).

[42] M. Methfessel and A. T. Paxton, Phys. Rev. B **40**, 3616 (1989).

[43] R. E. Voskoboinikov and C. M. F. Rae, IOP Conf. Ser.: Mater. Sci. Eng. **3**, 012009 (2009).

[44] W. Wang, C. B. Jiang, and K. Lu, Acta Mater. **51**, 6169 (2003).

[45] Y. Chiu and A. H. Ngan, Acta Mater. **50**, 1599 (2002).

[46] K. Xiong, H. Lu, and J. Gu, Comput. Mater. Sci. **115**, 214 (2016).

[47] S. Kohlhammer, M. Fähnle, and G. Schoeck, Scr. Mater. **39**, 359 (1998).

[48] S. Qin, S.-L. Shang, J. Shimanek, Z.-K. Liu, and A. M. Beese (unpublished).

[49] R. Maaß, L. Meza, B. Gan, S. Tin, and J. R. Greer, Small **8**, 1869 (2012).

[50] S. L. Shang, A. Saengdeejing, Z. G. Mei, D. E. Kim, H. Zhang, S. Ganeshan, Y. Wang, and Z. K. Liu, Comput. Mater. Sci. **48**, 813 (2010).

[51] S. Ogata, J. Li, and S. Yip, Science **298**, 807 (2002).

[52] P. N. H. Nakashima, A. E. Smith, J. Etheridge, and B. C. Muddle, Science **331**, 1583 (2011).

[53] L. G. Hector, J. F. Herbst, and T. W. Capehart, J. Alloys Compd. **353**, 74 (2003).

[54] J. P. Hirth and J. Lothe, *Theory of Dislocations* (Krieger, Malabar, FL, 1992).

[55] D. E. Kim, S. L. Shang, and Z. K. Liu, Intermetallics **18**, 1163 (2010).

[56] V. E. Osswald, Z. Phys. A: Hadron. Nucl. **83**, 55 (1933).

[57] P. Haasen, Philos. Mag. **3**, 384 (1958).

[58] E. N. D. C. A. Andrade and C. Henderson, Philos. Trans. R. Soc. London A **244**, 177 (1951).

[59] D. M. Dimiduk, M. D. Uchic, and T. A. Parthasarathy, Acta Mater. **53**, 4065 (2005).

[60] F. E. Heredia and D. P. Pope, Acta Metall. Mater. **39**, 2027 (1991).

[61] T. Hirano, M. Demura, and D. Golberg, Acta Mater. **47**, 3441 (1999).

[62] W. G. Nöhring and W. A. Curtin, Acta Mater. **128**, 135 (2017).

[63] J. Xiao, H. Cui, H. Zhang, W. Wen, and J. Zhou, Mater. Sci. Eng.: A, doi:10.1016/j.msea.2019.138631 (2020).

[64] W. Zhu, D. Fort, I. P. Jones, and R. E. Smallman, Philos. Mag. Lett. **77**, 307 (1998).

[65] T. S. Rong, I. P. Jones, and R. E. Smallman, J. Phys. IV **03**, C7-457 (1993).

[66] S. Keshavarz and S. Ghosh, Philos. Mag. **95**, 2639 (2015).
[67] Y. Kamimura, K. Edagawa, A. M. Iskandarov, M. Osawa, Y. Umeno, and S. Takeuchi, Acta Mater. **148**, 355 (2018).
[68] K. Edagawa, Y. Kamimura, A. M. Iskandarov, Y. Umeno, and S. Takeuchi, Materialia **5**, 100218 (2019).
[69] Y. Luo, J. Liu, W. Guo, Q. Yu, and S. Li, J. Dyn. Behav. Mater. **2**, 223 (2016).